

# Gravitational waves from extreme-mass-ratio inspirals using general parametrized metrics

Shuo Xin,<sup>1,2</sup> Wen-Biao Han,<sup>1,3,\*</sup> and Shu-Cheng Yang<sup>1,3</sup>

<sup>1</sup>*Shanghai Astronomical Observatory, Shanghai, 200030, China*

<sup>2</sup>*School of Physics Sciences and Engineering, Tongji University, Shanghai 200092, China*

<sup>3</sup>*School of Astronomy and Space Science, University of Chinese Academy of Sciences, Beijing, 100049, China*



(Received 17 December 2018; revised manuscript received 5 September 2019; published 25 October 2019)

Future space-borne interferometers will be able to detect gravitational waves at  $10^{-3}$  to  $10^{-1}$  Hz. In this band extreme-mass-ratio inspirals (EMRIs) can be promising gravitational-wave sources. In this paper, we investigate the possibility of testing the hypothesis that the small body is moving in Kerr spacetime against the alternative that the small body is moving in a parametrized non-Kerr metric by matching gravitational waveforms. EMRI snapshots from either equatorial geodesics or inclined geodesics suffer from the “confusion problem.” Our results show that, within the time scale before significant (radiation-driven) orbital evolution takes place, small and moderate deviations from the Kerr spacetime [ $|\delta_i| < 1$  in the notation of Ni, Jiang, and Bambi *J. Cosmol. Astropart. Phys.* **09** (2016) 014] can be discerned only when the Kerr spin parameter is extreme. In geodesic cases, most waveforms related to a non-Kerr metric can be mimicked by the waveform templates produced from a Kerr black hole. However, when radiation reaction is taken into consideration, the signals that are originally degenerate with each other will gradually separate and finally break the confusion. Depending on the mass ratio and other parameters of the system, the time needed to break the degeneracy can vary from several hours to several months.

DOI: [10.1103/PhysRevD.100.084055](https://doi.org/10.1103/PhysRevD.100.084055)

## I. INTRODUCTION

LIGO’s detection of the black hole (BH) merger event GW150914 has opened the era of gravitational-wave (GW) astronomy [1]. The observation of GW170817 [2] and its electromagnetic counterpart led to multimessenger astronomy [3]. Electromagnetic observations have deepened our understanding of the Universe since the birth of astronomy and the new messenger—gravitational waves—might bring more discoveries. With ground-based detectors [4,5], space interferometers [6], and pulsar-timing arrays [7] we may observe merger events, EMRIs, primordial GWs, etc. These observations, which were previously inaccessible, could potentially deepen our understanding of the Universe and fundamental physics.

Current ground-based gravitational-wave detectors are able to detect GWs in a relatively high frequency band. The Laser Interferometer Space Antenna (LISA [8]), Taiji [9], and TianQin [10], planned to launch in 2030s, will extend the observation band down to the millihertz range. LISA *Pathfinder* has demonstrated the desired accuracy in its noise spectrum [11], and future LISA missions could yield important scientific discoveries. By analyzing GW signals in the LISA band, we can study the merger history

of BHs [12], probe stellar dynamics [13], and test gravity theories [14].

An extreme-mass-ratio inspiral (EMRI), e.g., a stellar-mass compact object ( $1 - 10 M_{\odot}$ ) orbiting around a supermassive black hole, is a promising source of GW signals in the LISA band [15–17]. Although a relatively accurate method to generate waveforms, the Teukolsky-based method [18–23] is computationally expansive. Some further approximations, i.e., numerical kludge [24], analytic kludge [25] etc., have made the calculation feasible. The analysis of EMRI signals is also sophisticated. Due to the low signal-to-noise ratio, matched filtering has to be utilized in the analysis, and both generating waveform templates and matching signals require enormous computational power. Markov chain Monte Carlo and machine learning methods might shed some light on this problem [26,27].

One scientific goal of LISA is to test general relativity and the Kerr metric in the strong-field regime, e.g., around BHs. Several previous works have demonstrated possible constraints that LISA can set on alternative metrics or theories of gravity. Reference [28] determined the bound that LISA can set on the coupling constant  $\omega$  in scalar-tensor theory. Reference [29] studied the influence of the BH quadrupole moment, and Ref. [30] gave estimated the parameter limits of the “bumpy BH metric” constrained by EMRI detection. A summary of previous works on possible

\*wbhan@shao.ac.cn

tests of gravity theories using LISA can be found in Ref. [31].

The “confusion problem” is one challenge we may encounter in data analysis. One kind of confusion comes from white dwarf binaries and other unresolved sources, as studied in Ref. [32]. This kind of confusion is treated as noise and contributes to an increase in the noise spectrum. Another kind of confusion is intrinsic to the model, namely, two EMRI waveforms with different parameters can be almost identical, which is the “stealth Bias” analyzed in Refs. [33,34]. By “identical” we mean that their overlap (as defined in the Sec. III) is over 0.97. Both kinds of confusion problems were discussed in previous works [29,31–33]. They can be approximately accounted for in the Fisher matrix analysis of error estimation. However, the second kind of confusion can be hard to analyze when the two confused signals are relatively far away in parameter space, before enough observation time has passed so that the radiation reaction might break the confusion.

The stealth bias was demonstrated in an early work [35] for a special case, i.e., in an approximate metric describing a BH + torus and the Kerr metric, the confusion problem exists for gravitational-wave emission from equatorial orbits, before radiation reaction becomes significant. However, as suggested in Ref. [33], a parametrized post-Einsteinian framework should be adopted when treating systems with such a stealth bias. Therefore, we extended the analysis to a continuously parametrized metric and general inclined eccentric orbits. Our results show that the confusion problem still exists for general geodesics. However, as stated in Refs. [29,31], radiation reaction could play the role of breaking the confusion and our results for orbits with evolution induced by radiation reaction are consistent with this. The degeneracy between signals can be broken within a few hours or a few months in the situations we have considered, depending on the mass ratio. On the other hand, we expect that the signals from extremely small-mass-ratio systems will stay confused with

the Kerr signal for several months. Systems with mass ratios lower than  $10^{-8}$  may exist in astrophysical environments and be observable [36,37].

In order to test the no-hair theorem, i.e., astrophysical BHs are described only by mass and spin, many methods of model-independent parametrization for BH metrics have been proposed. The Johannsen-Psaltis (JP) metric [38] and the Johannsen metric [39], which expand the metric component in power series of  $\frac{M}{r}$ , are widely used in testing Kerr hypothesis. However, as mentioned in Ref. [40], the Johannsen metric has some convergence deficiencies in the strong-field regime. Such a problem can be solved by the Konoplya-Rezzolla-Zhidenko (KRZ) parametrization proposed in Ref. [41], which expands the metric functions in power series of  $\cos\theta$ . Here we apply the lowest-order KRZ metric and adopt the choice of deformation parameters used in Ref. [42], which also studied the Kerr metric.

The rest of this paper is organized as follows. In Sec. II a general parametrization for BH spacetime is discussed. Section III introduces the “kludge” waveform generation method and matched filtering procedure that use. Then, in Sec. IV we present our results about the “confusion” problem. Finally, we summarize and discuss the results in Sec. V.

## II. GENERAL PARAMETRIZATION OF THE METRIC AROUND A BLACK HOLE

In order to test the Kerr hypothesis or general relativity in a model-independent manner, one usually turns to a general parametrization of the metric describing astrophysical BHs. Instead of using a metric derived from a specific theory, a general metric could enable model-independent tests of the Kerr hypothesis. One reasonable choice is to expand the metric functions in power series of  $\frac{1}{r^2+a^2\cos^2\theta}$ , as adopted by Johannsen and Psaltis. [38]. In Boyer-Lindquist coordinates, the metric—which we refer to as the JP metric—reads

$$ds^2 = -[1 + h(r, \theta)] \left(1 - \frac{2Mr}{\Sigma}\right) dt^2 - \frac{4aMr \sin^2\theta}{\Sigma} [1 + h(r, \theta)] dt d\phi + \frac{\Sigma[1 + h(r, \theta)]}{\Delta + a^2 \sin^2\theta h(r, \theta)} dr^2 + \Sigma d\theta^2 + \left[ \sin^2\theta \left( r^2 + a^2 + \frac{2a^2 Mr \sin^2\theta}{\Sigma} \right) + h(r, \theta) \frac{a^2(\Sigma + 2Mr) \sin^4\theta}{\Sigma} \right] d\phi^2, \quad (1)$$

where

$$\Sigma = r^2 + a^2 \cos^2\theta, \quad \Delta = r^2 - 2Mr + a^2, \quad h(r, \theta) = \sum_{k=0}^{\infty} \left( \epsilon_{2k} + \epsilon_{2k+1} \frac{Mr}{\Sigma} \right) \left( \frac{M^2}{\Sigma} \right)^k. \quad (2)$$

When testing the Kerr metric, one usually hopes that the alternative metric still preserves the symmetries of the Kerr metric, which are related to three constants of motion. A general form of the metric that has three constants of motion was proposed by Johannsen [39]. The line element of this parametrization in Boyer-Lindquist coordinates—which we refer to as the Johannsen metric—is

$$ds^2 = -\frac{\tilde{\Sigma}[\Delta - a^2 A_2(r)^2 \sin^2 \theta]}{[(r^2 + a^2)A_1(r) - a^2 A_2(r) \sin^2 \theta]^2} dt^2 - \frac{a[(r^2 + a^2)A_1(r)A_2(r) - \Delta]\tilde{\Sigma} \sin^2 \theta}{[(r^2 + a^2)A_1(r) - a^2 A_2(r) \sin^2 \theta]^2} dt d\phi$$

$$+ \frac{\tilde{\Sigma} \sin^2 \theta [(r^2 + a^2)^2 A_1(r)^2 - a^2 \Delta \sin^2 \theta]}{[(r^2 + a^2)A_1(r) - a^2 A_2(r) \sin^2 \theta]^2} d\phi^2 + \frac{\tilde{\Sigma}}{\Delta A_5(r)} dr^2 + \tilde{\Sigma} d\theta^2, \quad (3)$$

where  $\Delta$  is defined in the same way as for the JP metric, and the functions  $A_i(r)$ ,  $i = 1, 2, 5$  and  $\tilde{\Sigma}$  are expanded in power series of  $\frac{M}{r}$ ,

$$A_i(r) = 1 + \sum_{n=2}^{\infty} \alpha_{in} \left(\frac{M}{r}\right)^n,$$

$$\tilde{\Sigma} = \Sigma + f(r),$$

$$f(r) = \sum_{n=3}^{\infty} \epsilon_n \frac{M^n}{r^{n-2}}. \quad (4)$$

The Johannsen metric and JP metric were adopted in several works that tested the Kerr metric, utilizing the iron

line [43,44], x-ray polarization [45], and black hole shadows [46]. However, as mentioned in Refs. [40,41], the Johannsen metric has several deficiencies. One major problem is expanding the function in power series of  $1/r$ , so that all elements in the series are almost equally important near the horizon, which puts a burden on testing the Kerr hypothesis in the strong-field regime. As we will discuss in Sec. IV, we have to study the dynamics as close to the horizon as possible to mitigate the ‘‘confusion.’’ This convergence problem can be solved by expanding the metric functions in power series of  $\cos \theta$ , as done in Ref. [41]. The line element around an axisymmetric black hole proposed by Konoplya, Rezzolla, and Zhidenko—which we refer to as the KRZ metric—is [41]

$$ds^2 = -\frac{N^2(\tilde{r}, \theta) - W^2(\tilde{r}, \theta) \sin^2 \theta}{K^2(\tilde{r}, \theta)} dt^2 - 2W(\tilde{r}, \theta) \tilde{r} \sin^2 \theta dt d\phi$$

$$+ K^2(\tilde{r}, \theta) \tilde{r}^2 \sin^2 \theta d\phi^2 + \Sigma(\tilde{r}, \theta) \left( \frac{B^2(\tilde{r}, \theta)}{\tilde{r}^2 N^2(\tilde{r}, \theta)} d\tilde{r}^2 + d\theta^2 \right), \quad (5)$$

where  $\tilde{r} = r/M$ ,  $\tilde{a} = a/M$ ,  $\Sigma$  is defined the same as in the JP metric, and the functions  $K(\tilde{r}, \theta)$ ,  $N(\tilde{r}, \theta)$ ,  $W(\tilde{r}, \theta)$ , and  $B(\tilde{r}, \theta)$  can be expanded in power series of  $\cos \theta$ . Here we use the same deformation parameter as in Ref. [42], namely,  $\delta_i$ ,  $i = 1, 2, 3, 4, 5, 6, 7, 8$  which is related to the metric functions by

$$N^2 = (1 - r_0/\tilde{r})[1 - \epsilon_0 r_0/\tilde{r} + (k_{00} - \epsilon_0) r_0^2/\tilde{r}^2 + \delta_1 r_0^3/\tilde{r}^3]$$

$$+ \left\{ a_{20} r_0^3/\tilde{r}^3 + a_{21} r_0^4/\tilde{r}^4 + k_{21} r_0^3/\tilde{r}^3 \left[ 1 + \frac{k_{22}(1 - r_0/\tilde{r})}{1 + k_{23}(1 - r_0/\tilde{r})} \right]^{-1} \right\} \cos^2 \theta, \quad (6)$$

$$B = 1 + \delta_4 r_0^2/\tilde{r}^2 + \delta_5 r_0^2 \cos^2 \theta/\tilde{r}^2, \quad (7)$$

$$W = [w_{00} r_0^2/\tilde{r}^2 + \delta_2 r_0^3/\tilde{r}^3 + \delta_3 r_0^3/\tilde{r}^3 \cos^2 \theta]/\Sigma, \quad (8)$$

$$K^2 = 1 + aW/r + \left\{ k_{00} r_0^2/\tilde{r}^2 + k_{21} r_0^3/\tilde{r}^3 \left[ 1 + \frac{k_{22}(1 - r_0/\tilde{r})}{1 + k_{23}(1 - r_0/\tilde{r})} \right]^{-1} \cos^2 \theta \right\} / \Sigma, \quad (9)$$

$$r_0 = 1 + \sqrt{1 - \tilde{a}^2}, \quad a_{20} = 2\tilde{a}^2/r_0^3, \quad a_{21} = -\tilde{a}^4/r_0^4 + \delta_6, \quad \epsilon_0 = (2 - r_0)/r_0, \quad k_{00} = \tilde{a}^2/r_0^2,$$

$$k_{21} = \tilde{a}^4/r_0^4 - 2\tilde{a}^2/r_0^3 - \delta_6, \quad w_{00} = 2\tilde{a}/r_0^2, \quad k_{22} = -\tilde{a}^2/r_0^2 + \delta_7, \quad k_{23} = \tilde{a}^2/r_0^2 + \delta_8, \quad (10)$$

This is a lowest-order metric expression, as shown in the Appendix of Ref. [41], where we replace  $a_{01}$ ,  $w_{01}$ ,  $w_{21}$ ,  $b_{01}$ , and  $b_{21}$  with  $\delta_1$ ,  $\delta_2$ ,  $\delta_3$ ,  $\delta_4$ , and  $\delta_5$ , respectively.  $\delta_1$  is related to the deformation of  $g_{tt}$ ,  $\delta_2$  and  $\delta_3$  are related to the rotational deformation, and  $\delta_4$  and  $\delta_5$  are related to the

deformation of  $g_{rr}$ . The KRZ parametrization only preserves stationarity and axisymmetry. When each  $\delta_i$  is set to 0, we recover the Kerr metric. In this paper we mainly consider the influence of  $\delta_1$  and  $\delta_2$ . To get a sense of the influence of the deformation parameters, in Fig. 1 we plot

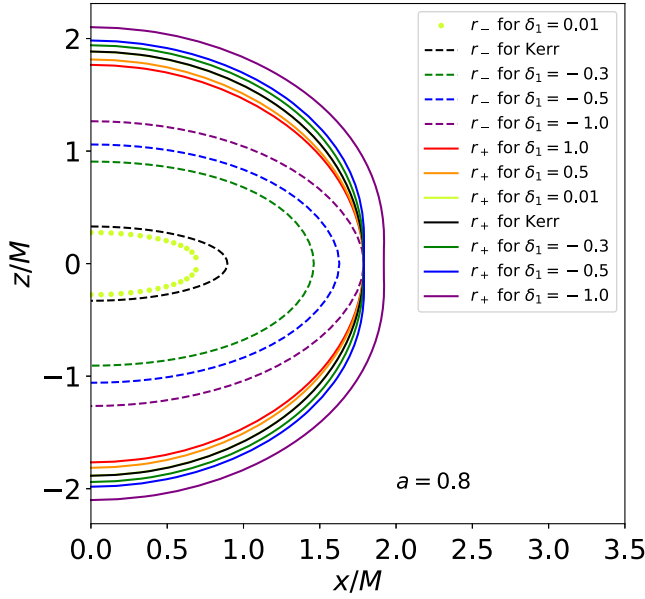


FIG. 1. Event horizon in the  $xz$  plane with the influence of  $\delta_1$ , where  $x \equiv \sqrt{r^2 + a^2} \sin \theta \cos \phi$  and  $z \equiv r \cos \theta$ . The dashed lines of different colors indicate the inner horizon  $r_-$ , and the solid lines indicate the outer horizon  $r_+$ .

the horizon for different values of  $\delta_1$  with the spin parameter  $a = 0.8$ . The horizon is the location where  $g_{rr}$  diverges and in the KRZ metric this is equivalent to solving  $N^2 = 0$ . Although the inner horizon has no direct relation to our study, it is a strong indicator of a BH's deformation. The inner horizon will disappear when  $\delta_1$  has a slightly positive value.

### III. KLUDGE WAVEFORM AND SIGNAL ANALYSIS

In this section we review the kludge waveform generation method and signal analysis approach. Throughout this section, natural units ( $G = c = 1$ ) are assumed, greek letters ( $\mu, \nu, \sigma, \dots$ ) are used to stand for indices running from 0 to 3, and Einstein summation is assumed.

The numerical kludge method, proposed in Ref. [24], generates EMRI waveforms with radiation fluxes in a relatively fast and accurate way. The procedure is as follows. Regarding the stellar-mass object as a point particle, we first calculate the trajectory of the particle in a given metric by integrating the geodesic equations augmented with the radiation flux; then, we use the quadrupole formula to obtain the gravitational wave from the test-particle geodesics.

In our case, to calculate the geodesics we use

$$\dot{u}^\mu = -\Gamma_{\rho\sigma}^\mu u^\rho u^\sigma, \quad (11)$$

$$\dot{x}^\mu = u^\mu, \quad (12)$$

where  $x^\mu$  is the Boyer-Lindquist coordinate of the particle,  $u^\mu$  is the 4-velocity, and  $\Gamma_{\rho\sigma}^\mu$  is the Christoffel connection. We do not use the conservation of particle mass, energy, and angular momentum to reduce the equations, but rather to monitor numerical error. Specifically, at each step of integration we check the conservation quantities, namely, the modulus of the 4-velocity, the energy  $E$ , and the  $z$  component of angular momentum  $L_z$ , defined by

$$|u| = -1 = g_{\mu\nu} u^\mu u^\nu, \quad (13)$$

$$E = -u_t = -g_{tt} u^t - g_{t\phi} u^\phi, \quad (14)$$

$$L_z = u_\phi = g_{t\phi} u^t + g_{\phi\phi} u^\phi. \quad (15)$$

In Kerr cases, we also check the Carter constant [47],

$$Q = (g_{\theta\theta} u^\theta)^2 + \cos^2 \theta \left( a^2 (\eta^2 - E^2) + \left( \frac{L_z}{\sin \theta} \right)^2 \right). \quad (16)$$

During the calculation, we keep the relative drift of conserved quantities within  $10^{-7}$ .

For stable bounded geodesics in Kerr spacetime, three parameters—the eccentricity  $e$ , semilatus  $p$ , and inclination angle  $\iota$ —can be used to characterize an orbit. They are defined by

$$e = \frac{r_a - r_p}{r_a + r_p}, \quad p = \frac{2r_a r_p}{r_a + r_p}, \quad \iota = \frac{\pi}{2} - \theta_{\min}, \quad (17)$$

where  $r_a$  is apastron,  $r_p$  is periastron, and  $\theta_{\min}$  is the minimum of the  $\theta$  coordinate along the geodesics. In Kerr spacetime, we can determine the three orbital parameters  $e$ ,  $p$ ,  $\iota$  from the three conserved quantities  $E$ ,  $L_z$ ,  $Q$  and vice versa [48]. In KRZ non-Kerr spacetime, we continue to use these definitions, i.e., for a numerically generated trajectory we still define  $(e, p, \iota)$  from  $(r_a, r_p, \theta_{\min})$  by the relation above.

For inclined orbits in Kerr spacetime, the relation between  $(r_a, r_p, \theta_{\min})$  and  $(E, L_z, Q)$  is given by [see Eqs. (30) and (31) in Ref. [48]]

$$P^2|_{r=r_a, \theta=\pi/2} - (r^2 + (L_z - aE)^2 + Q)\Delta|_{r=r_a, \theta=\pi/2} = 0, \quad (18)$$

$$P^2|_{r=r_p, \theta=\pi/2} - (r^2 + (L_z - aE)^2 + Q)\Delta|_{r=r_p, \theta=\pi/2} = 0, \quad (19)$$

$$Q = \cos^2 \theta_{\min} \left( a^2 (1 - E^2) + \frac{L_z^2}{\sin^2 \theta_{\min}} \right), \quad (20)$$

where  $P = E(r^2 + a^2) - aL_z$  and  $\Delta = r^2 - 2Mr + a^2$ .

For equatorial orbits in a stationary and axisymmetric general metric, we can analytically determine  $e$ ,  $p$  from  $E$ ,  $L_z$  and vice versa by the relation ( $|u| = -1$  with  $u_r = 0$  at apastron and periastron)

$$\begin{aligned} g^{tt}|_{r=r_a, \theta=\pi/2} E^2 + g^{\phi\phi}|_{r=r_a, \theta=\pi/2} L_z^2 - 2g^{t\phi}|_{r=r_a, \theta=\pi/2} E L_z &= -1, \\ g^{tt}|_{r=r_p, \theta=\pi/2} E^2 + g^{\phi\phi}|_{r=r_p, \theta=\pi/2} L_z^2 - 2g^{t\phi}|_{r=r_p, \theta=\pi/2} E L_z &= -1. \end{aligned} \quad (21)$$

The effect of radiation reaction is included by replacing Eq. (11) with

$$\frac{du^\mu}{d\tau} = -\Gamma_{\rho\sigma}^\mu u^\rho u^\sigma + \mathcal{F}^\mu, \quad (22)$$

where the radiation force  $\mathcal{F}^\mu$  is recovered from the adiabatic radiation fluxes ( $\dot{E}$ ,  $\dot{L}_z$ ,  $\dot{Q}$ ) as

$$\begin{aligned} \dot{E}u^t &= -g_{tt}\mathcal{F}^t - g_{t\phi}\mathcal{F}^\phi, \\ \dot{L}_z u^t &= g_{t\phi}\mathcal{F}^t + g_{\phi\phi}\mathcal{F}^\phi, \\ \dot{Q}u^t &= 2g_{\theta\theta}^2 u^\theta \mathcal{F}^\theta + 2\cos^2\theta a^2 E \dot{E} + 2\cos^2\theta \frac{L_z \dot{L}_z}{\sin^2\theta}, \\ g_{\mu\nu} u^\mu \mathcal{F}^\nu &= 0. \end{aligned} \quad (23)$$

We use the flux expressions of the second post-Newtonian approximations with the corrections described

in Ref. [24]. Equation (23) can be deduced by taking derivatives with respect to proper time in Eqs. (13)–(16).

After generating the trajectory, we transform  $(r, \theta, \phi)$  into  $(x, y, z)$  using the definition of spherical coordinates (rather than the Boyer-Lindquist coordinates), namely,  $x = r \sin \theta \cos \phi$ ,  $y = r \sin \theta \sin \phi$ , and  $z = r \cos \theta$ . Then we use the quadrupole formula, i.e.,

$$\bar{h}^{jk}(t, x) = \frac{2}{r} [\ddot{T}^{jk}(t')]_{t'=t-r}, \quad (24)$$

$$I^{jk} = \mu x^j_p x^k_p, \quad (25)$$

where  $\bar{h}^{\mu\nu} = h^{\mu\nu} - \frac{1}{2}\eta^{\mu\nu}\eta^{\rho\sigma}h_{\rho\sigma}$  is the trace-reversed metric perturbation.

We transform the waveform into transverse-traceless gauge [see Eqs. (17) and (23) in Ref. [24]] and we get the plus and cross components of the waveform observed at latitudinal angle  $\Theta$  and azimuthal angle  $\Phi$ :

$$\begin{aligned} h_+ &= h^{\Theta\Theta} - h^{\Phi\Phi} \\ &= \{\cos^2\Theta[h^{xx}\cos^2\Phi + h^{xy}\sin 2\Phi h^{yy}\sin^2\Phi] + h^{zz}\sin^2\Theta - \sin 2\Theta[h^{xz}\cos\Phi + h^{yz}\cos\Phi]\} \\ &\quad - [h^{xx}\sin^2\Phi - h^{xy}\sin 2\Phi + h^{yy}\cos^2\Phi], \end{aligned} \quad (26)$$

$$\begin{aligned} h_\times &= 2h^{\Theta\Phi} \\ &= 2\left\{\cos\Theta\left[-\frac{1}{2}h^{xx}\sin 2\Phi + h^{xy}\cos 2\Phi + \frac{1}{2}h^{yy}\sin 2\Phi\right] + \sin\Theta[h^{xz}\sin\Phi - h^{yz}\cos\Phi]\right\}. \end{aligned} \quad (27)$$

With these ‘‘plus’’ and ‘‘cross’’ components, we define our waveforms as  $h = h_+ + ih_\times$ .

Matched filtering is the standard technique used in LISA analyses. In real EMRI data analyses, a large bank of waveform templates will be compared with the detected signal to find the matched template. Here we mainly adopt the fitting factor as a measure of similarity between two waveforms within the LISA band.

The inner product between a signal  $a(t)$  and a template  $b(t)$  is defined by their cross correlation [49],

$$(a|b) = 4\Re \int \frac{\tilde{a}^*(f)\tilde{b}(f)}{S_n(f)} df = 2 \int \frac{\tilde{a}^*(f)\tilde{b}(f) + \tilde{a}(f)\tilde{b}^*(f)}{S_n(f)} df, \quad (28)$$

where  $S_n(f)$  is the power spectral density of LISA noise. In our calculation, the analytic fit to the noise spectrum is the same as that used in Ref. [24].

The overlap (fitting factor) between the signal and template is defined as [50]  $\text{FF}(a, b) = \frac{(a|b)}{\sqrt{(a|a)(b|b)}}$ . It is worth noting that the standard fitting factor should be maximized over both time and phase shift. The fitting factor defined by time shift  $t_s$  and phase shift  $\phi_s$  is  $\text{ff}(t_s, \phi_s, a(t), b(t)) = \frac{(a(t)|b(t+t_s)e^{i\phi_s})}{\sqrt{(a|a)(b|b)}}$ . So the maximized fitting factor should be [51]

$$\text{FF}(a, b) = \max_{t_s, \phi_s} \frac{|a|b(t + t_s)e^{i\phi_s}|}{\sqrt{|a|}|b|}. \quad (29)$$

In the present work, we directly use the match function from the PyCBC Library [52]. When the overlap between two waveforms is above 0.97, we say that the waveform of this template is discovered in the signal. However, if a non-Kerr signal has an overlap with a Kerr template above 0.97, we could mistake the signal as being emitted from around a Kerr BH, i.e., the confusion problem mentioned in Ref. [13].

A weaker criterion ( $\text{FF} > 0.95$ ) was used in Ref. [13] when estimating the confusion. The limit adopted in template generation methods is 0.97 [48] or 0.99 [53], where the approximated models are believed to be faithful enough to more accurate fiducial models if the resulting waveforms have overlaps of over 0.97 or 0.99. However, as can be seen in Sec. IV, whether we choose 0.95, 0.97, or 0.99 does not substantially affect the conclusions. The overlap achieved by varying  $(M, a)$  is larger than 0.99 in most of the parameter space, but that achieved by varying  $(e, p)$  is less than 0.9 in orbits with parameters close to the last stable orbit (or more precisely, as shown in Fig. 4, the overlap becomes lower as we go from the upper right to the lower left part of the  $e$ - $p$  plane.), while the overlap quickly drops below 0.8 when changing the parameter by about 0.1% without matching orbital frequencies.

## IV. NUMERICAL RESULTS AND ANALYSIS

When we try to identify short EMRI signals, the confusion problem (as described in Ref. [13]) could prevent us from discerning non-Kerr and Kerr signals. Namely, an overlap over 0.97 might exist between non-Kerr and Kerr signals with certain parameters. However, this confusion can be eliminated by taking radiation reaction into consideration. In Secs. IV A and IV B we show the confusion problem when matching gravitational waveforms from equatorial and inclined geodesic orbits. In Sec. IV C we show the effect of radiation reaction on breaking the degeneracy.

### A. Equatorial geodesic orbit

Given a waveform in a spacetime with nonzero deformation, determining whether the “confusion problem” exists by searching over the entire parameter space would be computationally impossible. A better way is to have some idea about which waveform in Kerr spacetime is most similar to the non-Kerr signal and look at their overlap. Here we search for the existence of confusion using a similar method to that in Ref. [35], i.e., we look at waveforms generated from geodesics with the same orbital frequency. The orbital frequencies in Kerr spacetime were given in Ref. [54]. In equatorial orbits, there are two frequencies  $\omega_\phi$  and  $\omega_r$  related to the motion of the  $\phi$  and  $r$  coordinates.

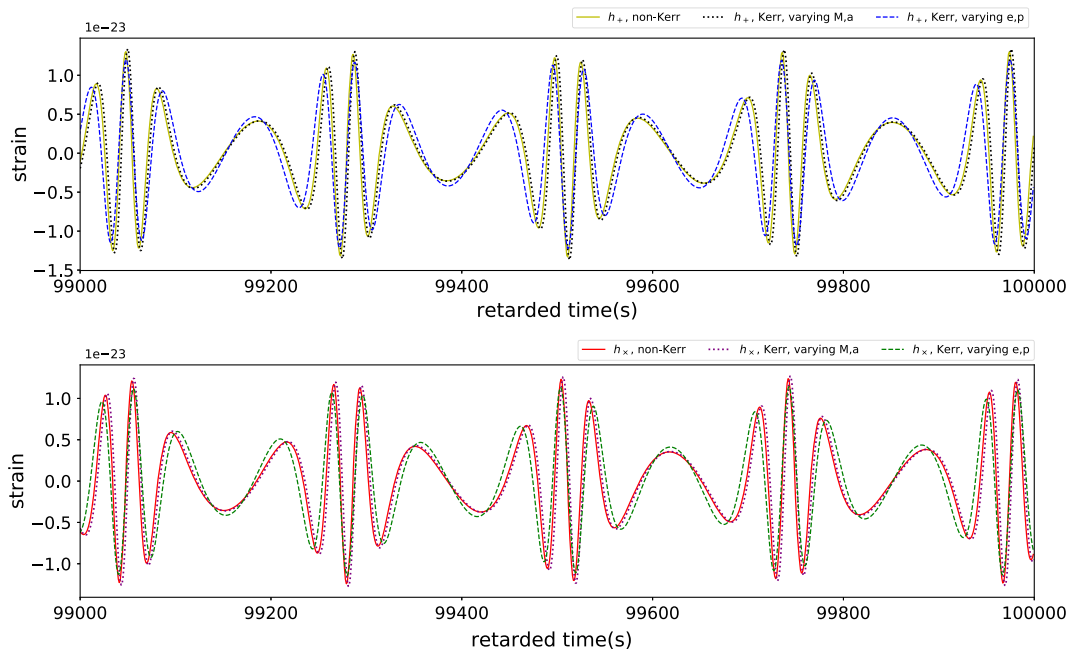


FIG. 2. “Plus” and “cross” components of gravitational waves emitted by equatorial orbits in non-Kerr and Kerr spacetimes, where we vary  $(M, a)$  or  $(e, p)$  to equate the orbital frequencies. The non-Kerr waveform is  $(\delta_1, a, M, e, p) = (0, 2, 0.5, 2 \times 10^5, 0.5, 6.0)$ . The yellow and red solid lines are the “plus” and “cross” components of the non-Kerr waveforms. The black and violet dotted lines are the “plus” and “cross” components of Kerr waveforms with the same orbital frequencies as non-Kerr orbits when varying  $(M, a)$ . The blue and green dashed lines are the “plus” and “cross” components of Kerr waveforms with the same orbital frequencies as non-Kerr orbits when varying  $(e, p)$ .

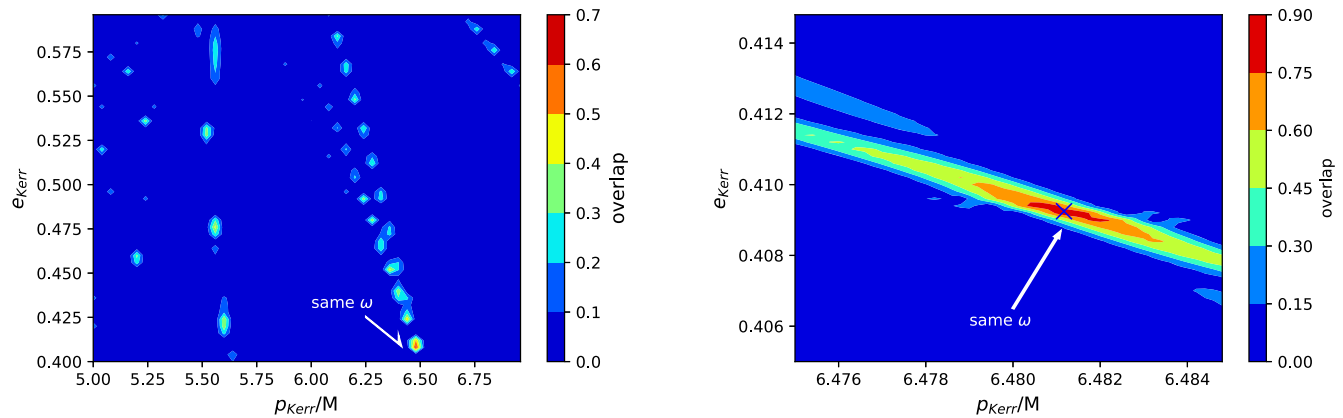


FIG. 3. Distribution of the overlap between waveforms defined by  $(\delta_1, a, M, e, p) = (0.2, 0.5, 2 \times 10^5, 0.5, 6)$  and  $(\delta_1, a, M, e, p) = (0, 0.5, 2 \times 10^5, e_{\text{Kerr}}, p_{\text{Kerr}})$  in the  $(e_{\text{Kerr}}, p_{\text{Kerr}})$  plane. The blue cross marks the same  $\omega_r$  and  $\omega_\phi$  at  $(e_{\text{Kerr}}, p_{\text{Kerr}}) = (0.409248, 6.481170)$ . The grid size is  $50 \times 50$ .

We set  $t_s = 0$ ,  $\phi_s = 0$  and use  $\text{ff}(0, 0, a(t), b(t))$  as a measure of degeneracy. Since  $\text{FF}(a, b) \geq \text{ff}(0, 0, a(t), b(t))$ , it is sufficient for the two signals to be degenerate if  $\text{ff}(0, 0, a(t), b(t)) > 0.97$ . In most cases,  $\text{ff}(0, 0, a(t), b(t))$  coincides with the maximum overlap when the initial conditions of the orbits are the same.

For equatorial motion, we set the initial  $t$  and  $\phi$  to 0 in view of stationarity and axisymmetry and set the initial  $r = r_{\text{max}}$ , so the orbit is uniquely determined by the orbital eccentricity  $e$ , semilatus rectum  $p$ , deformation parameters  $\delta_i$ , BH mass  $M$ , and BH spin  $a$ . As described in Ref. [35], we can achieve the same orbital frequency as non-Kerr orbits by varying the orbital parameters  $e$ ,  $p$  or BH parameters  $M$ ,  $a$ . So we need to consider orbits determined by  $(\delta, a, M, e, p)$ ,  $(0, a, M, e_{\text{Kerr}}, p_{\text{Kerr}})$ , and  $(0, a_{\text{Kerr}}, M_{\text{Kerr}}, e, p)$ . A comparison of waveforms generated by orbits with the same orbital frequency is shown in Fig. 2. We calculated the waveforms for 100 000 s (about 1 day), and in the figure we show a magnification around

the last 1000 s. The overlap between waveforms with varying BH mass and spin is over 0.99.

According to Ref. [13], orbits with the same orbital frequencies  $\omega_r$  and  $\omega_\phi$  can generate gravitational waveforms that could potentially be confused with non-Kerr signals. Therefore, the overlap between a non-Kerr waveform and several Kerr waveforms should have a local maximum around the parameter leading to the same orbital frequency. We checked this result by looking at overlaps between waveforms defined by  $(\delta_1, a, M, e, p) = (0.2, 0.5, 2 \times 10^5, 0.5, 6)$  and  $(\delta_1, a, M, e, p) = (0, 0.5, 2 \times 10^5, e_{\text{Kerr}}, p_{\text{Kerr}})$  with varying  $e_{\text{Kerr}}$  and  $p_{\text{Kerr}}$ . First we looked at the overlap distribution over a relatively large range of  $(e, p)$  and find that the highest local maximum is located around the point whose parameter values correspond to identical orbital frequencies. Then, we searched near  $(e_{\text{Kerr}}, p_{\text{Kerr}})$  with the same orbital frequency and found that the aforementioned point is approximately located at the peak of the overlap distribution, as shown in Fig. 3.

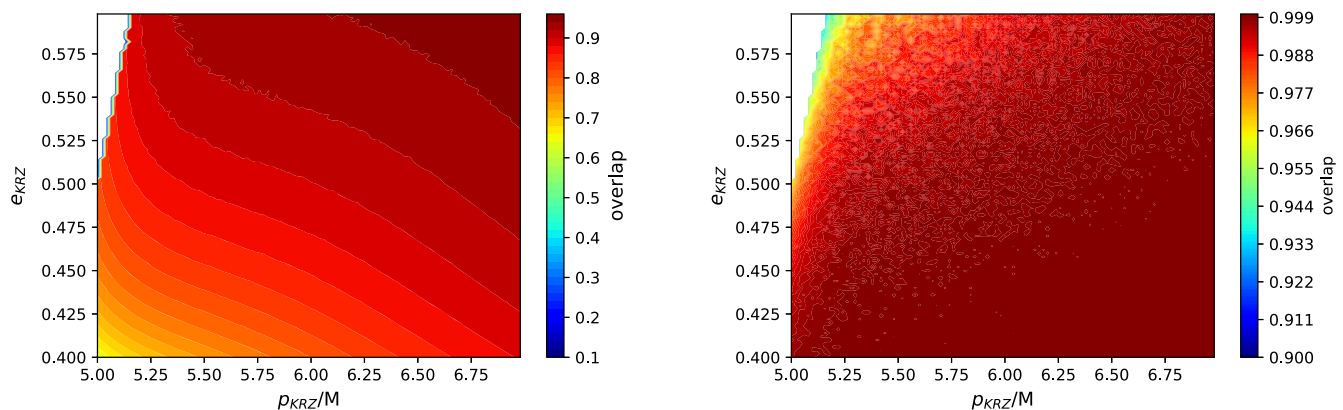


FIG. 4. Distribution of the overlap between waveforms with  $(\delta_1, a, M, e, p) = (0.2, 0.5, 2 \times 10^5, e_{\text{KRZ}}, p_{\text{KRZ}})$  and Kerr waveforms with identical  $\omega_r$  and  $\omega_\phi$  by varying  $e_{\text{Kerr}}, p_{\text{Kerr}}$  (left panel) and varying  $M, a$  (right panel) in the  $(e_{\text{KRZ}}, p_{\text{KRZ}})$  plane. The grid size is  $100 \times 100$ . The blank region contains unstable orbits.

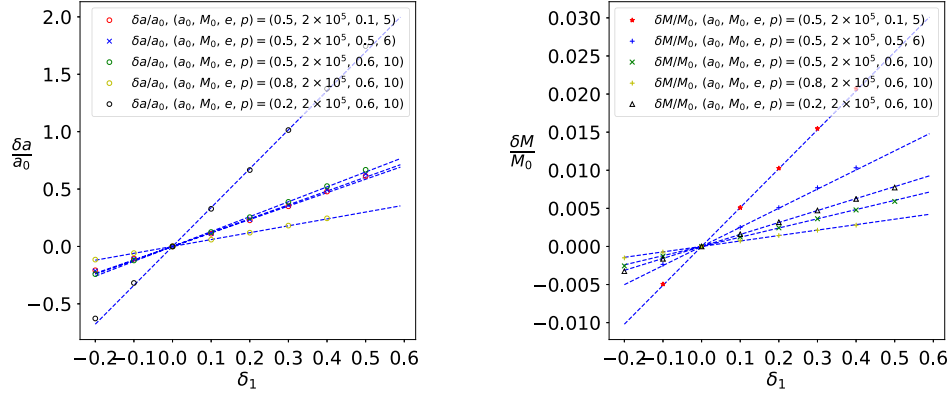


FIG. 5. Relation between the relative varying spin/mass values when equating the orbital frequencies, i.e., the orbits of  $(\delta_1, a_0, M_0, e, p)$  and  $(0, a_0 + \delta a, M_0 + \delta M, e, p)$  have the same orbital frequency in the  $\frac{\delta a}{a_0} - \delta_1$  (left) and  $\frac{\delta M}{M_0} - \delta_1$  (right) planes.

Then we investigated the confusion problems for different non-Kerr signals. First we studied the signals from different orbits, i.e., different  $e_{\text{KRZ}}$ ,  $p_{\text{KRZ}}$ . Since metric deformation is more evident near the BH horizon, we look at waveforms generated by trajectories close to the innermost bound orbit. We compare waveforms defined by  $(\delta_1, a, M, e, p) = (0.2, 0.5, 2 \times 10^5, e_{\text{KRZ}}, p_{\text{KRZ}})$  and Kerr orbits with the same orbital frequencies by varying  $(e, p)$  or  $(M, a)$  on a  $100 \times 100$  grid of  $(e, p)$ . Contour plots of the waveform overlap when varying  $(e, p)$  and  $(M, a)$

shown in Fig. 4. The confusion problem exists when varying  $(M, a)$  for most of the parameter region we considered.

Furthermore, the confusion problem exists for a large range of the deformation parameter. On top of that, when changing the deformation parameter, we found an almost linear relation between  $\delta_i$  and varied BH spin/mass ( $a_{\text{Kerr}}$  and  $M_{\text{Kerr}}$ ), as shown in Fig. 5 and 6. Since we are considering equatorial orbits, i.e.,  $\cos \theta = 0$ , only  $\delta_1$ ,  $\delta_2$ , and  $\delta_4$  can influence the results. Figure 7 shows that the

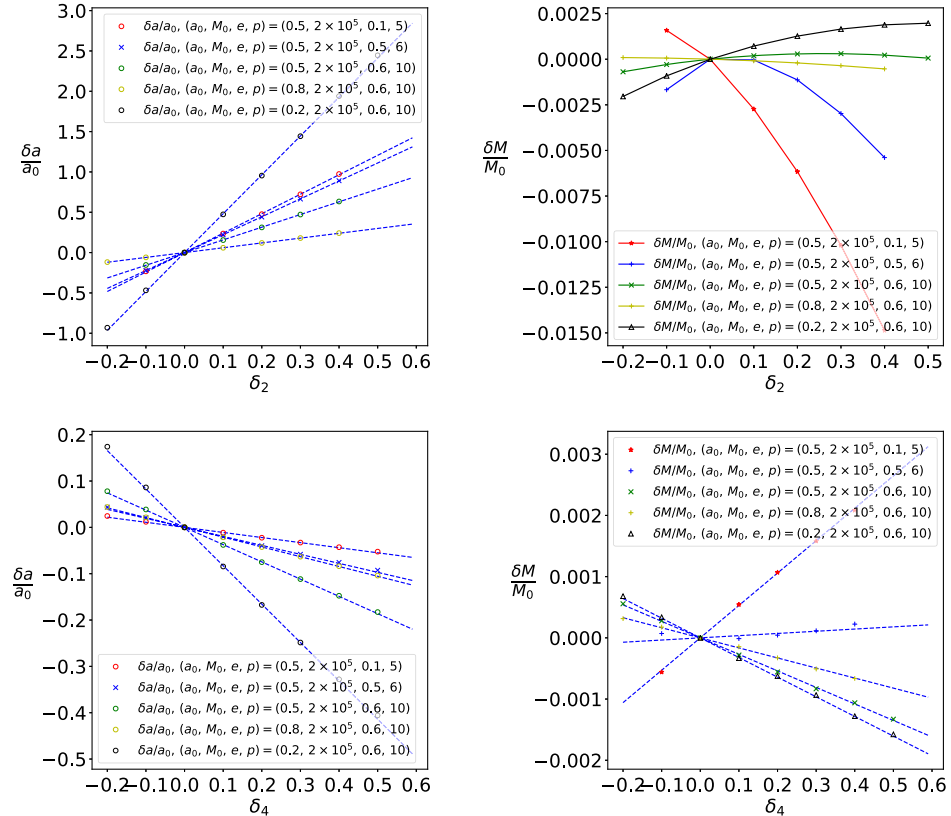


FIG. 6. The same as in Fig. 5, but for  $\delta_2$  (top panels) and  $\delta_4$  (bottom panels).

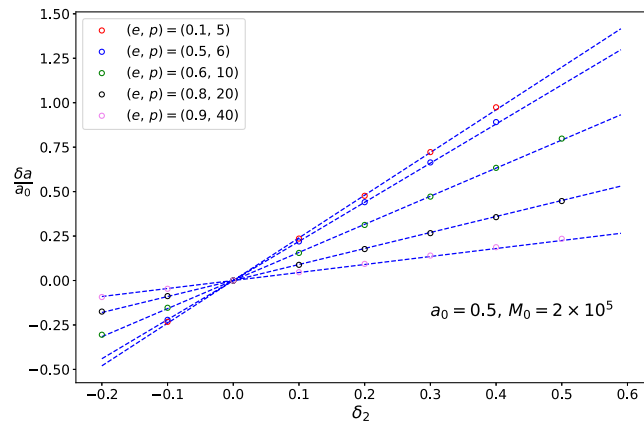


FIG. 7. The same as in Fig. 5, but only for the  $\delta a/a_0 - \delta_2$  relations for different orbits.

slope of this “linear” relation varies greatly for different  $(e, p)$ , so the relation is not a property intrinsic to the metric, but rather dependent on the orbit. The linearity is not a result of a small deformation. In fact, as shown in the figures above, the spin varies by up to 1–2 times the spin in the KRZ metric. The linearity does not hold for  $\delta M - \delta_2$ , but since it is not our major concern and the mass here is just a time scale, we did not explore this further.

Therefore, for given orbital parameters  $(e, p)$  we can regard the introduction of  $\delta_i$  as adding the black hole spin and mass proportionally. This sets a limit for the range of the deformation parameters within which we can vary  $(M_{\text{Kerr}}, a_{\text{Kerr}})$ . The upper limit is set by requiring  $a_{\text{Kerr}} < 1$  and the lower limit is set by requiring  $a_{\text{Kerr}} > 0$  or a stable orbit, e.g., for  $(e, p) = (0.5, 6.0)$ , when  $a_{\text{Kerr}}$  is small, the orbit is no longer stable and bounded. Figure 8 shows the

upper and lower bounds of the deformation parameters with respect to BH spin for orbits with  $e = 0.5$ ,  $p = 6.0$ .

## B. Inclined geodesic orbit

Equatorial orbits require some special conditions, i.e., the number of orbital frequencies is equal to the number of Kerr BH parameters. Therefore, in general we can solve for the mass and spin by equating the two frequencies determined by KRZ orbit, and the resulting geodesics are almost identical. However, no EMRIs will be perfectly equatorial. Instead, general EMRIs come from inclined orbits, which have three orbital frequencies. In such cases we usually cannot equate the three frequencies by only varying the BH parameters.

However, we found that by varying  $(M, a, p)$  to equate three orbital frequencies, the resulting gravitational waveforms also have an overlap over 0.97, even though the orbits are apparently not identical. The upper and middle panels of Fig. 9 show the time series of motion in the  $r$  and  $\theta$  directions and trajectories for the last 5000 s, where the total time is  $3 \times 10^6$  s. Motion in the  $\theta$  direction almost overlaps, but it has a few distortions. Motion in the  $r$  direction has the same frequency but different amplitude, which is basically due to varying the semilatus  $p$ . However, the gravitational-wave signals are almost identical, as shown in the bottom panel.

Similar to the equatorial cases, the requirements that  $a_{\text{Kerr}} < 1$  and that we have stable orbits set a bound on the deformation parameters. However, since there is no Carter-like constant in the KRZ metric, we cannot control the orbital parameters  $(e, p, i)$  in non-Kerr cases in simple ways. Therefore, we try to just control the initial conditions so that the orbital parameters are at least near the desired

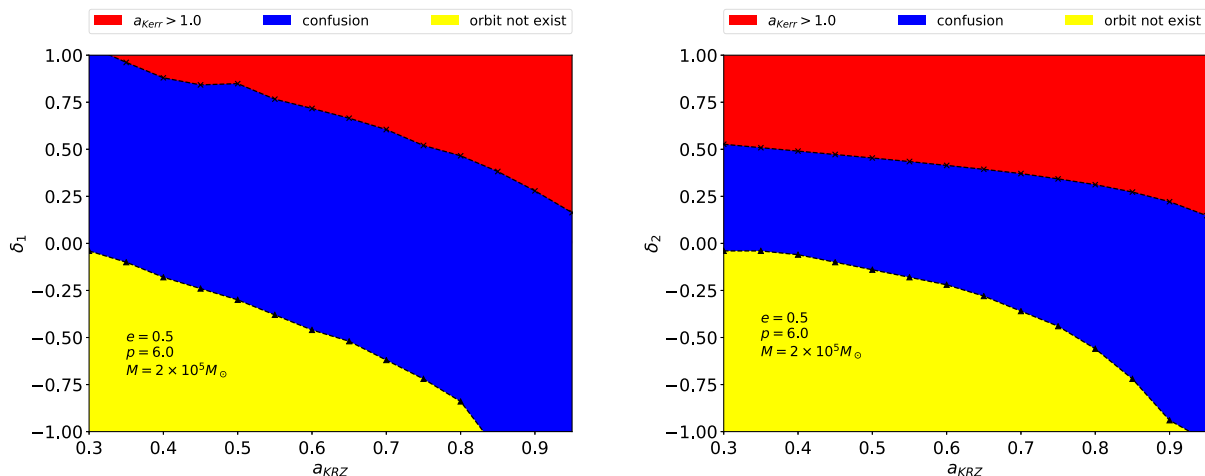


FIG. 8. Ranges of parameters that lead to degeneracy. The ranges are projected onto  $\delta_i$ - $a_{\text{KRZ}}$  parameter plane with other parameters set to  $e = 0.5$ ,  $p = 6.0$  and  $M = 2 \times 10^5$ . Each point on the plane indicates an EMRI system with  $e = 0.5$ ,  $p = 6.0$ ,  $M = 2 \times 10^5$  and  $\delta_i$ ,  $a_{\text{KRZ}}$  set by the coordinate in the plot. Colors are indexed as follows. Blue: the system is degenerate with another one in Kerr spacetime by frequency matching. Red: the corresponding system in Kerr spacetime by frequency matching has a spin larger than 1 ( $a_{\text{Kerr}} > 1$ ). Yellow: the system does not exist. Left panel: for  $\delta_1$  while  $\delta_2$  is set to 0. Right panel: for  $\delta_2$  while  $\delta_1$  is set to 0.

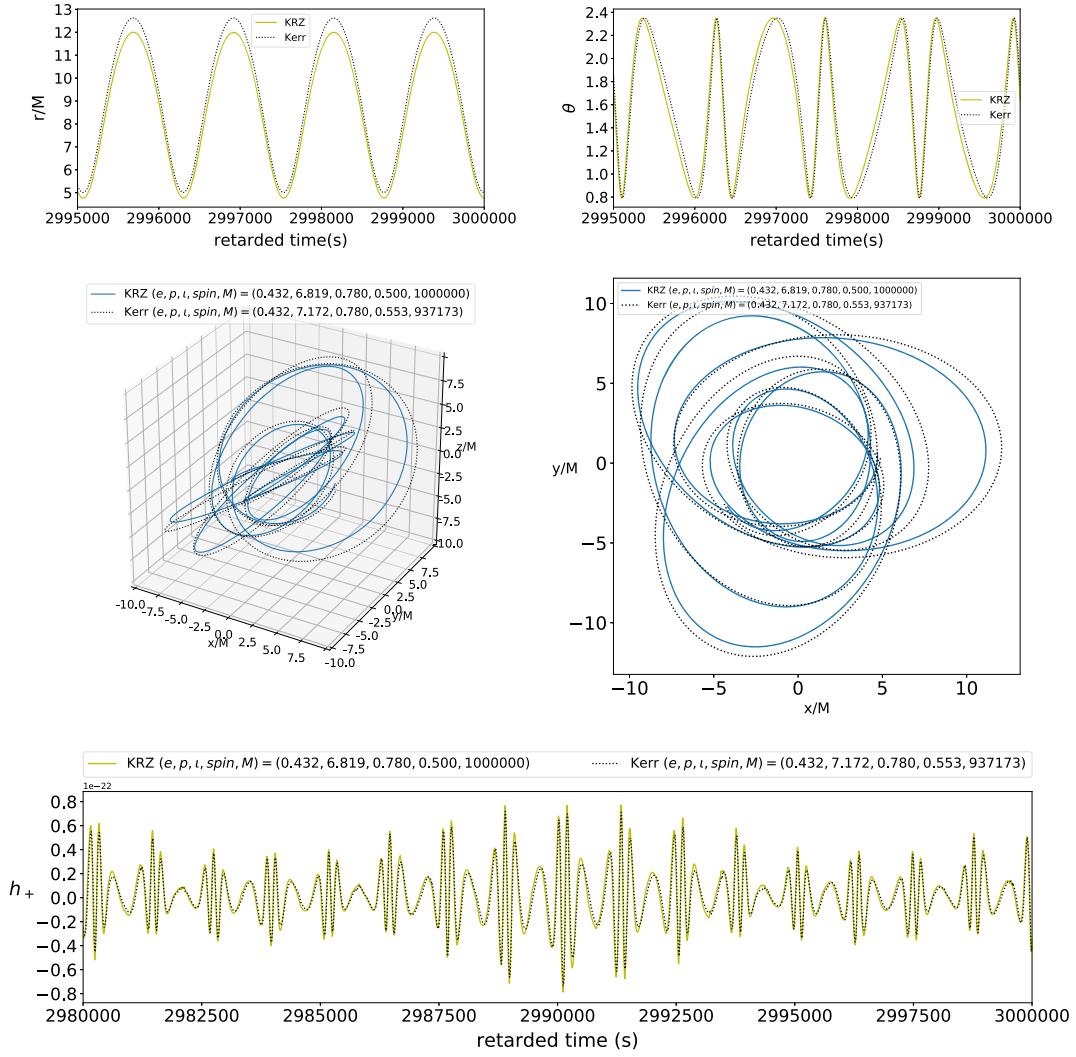


FIG. 9. Orbits and GW waveforms of a KRZ orbit and a Kerr orbit with the same orbital frequencies. Top left panel: Time series of motion in the  $r$  direction for the last 5000 s. Top right panel: Time series of motion in the  $\theta$  direction for the last 5000 s. Middle left panel: Trajectories for the last 5000 s. Middle right panel: Projection onto the  $x$ - $y$  plane of the trajectories for the last 5000 s. Bottom panel: “Plus” component of the EMRI waveform for the last 20 000 s. The orbital parameters and BH spin/mass are  $(e, p, \iota, \text{spin}, M) = (0.432, 6.819, 0.780, 0.5, 10^6)$ . The deformation parameter of the KRZ orbit is  $\delta_1 = 0.2$ .

values, e.g.,  $(e, p, \iota) = (0.2, 8, \pi/4)$ . Technically, given  $\delta_i$ ,  $a_{\text{KRZ}}$ , and the reference orbital parameters, we calculate the energy  $E_{\text{Kerr}}$  and angular momentum  $L_{z-\text{Kerr}}$  in Kerr spacetime with spin equal to  $a_{\text{KRZ}}$ ; then, we set the initial coordinates as  $\theta = \pi/2$ ,  $\phi = 0$ ,  $t = 0$ , and  $r = \frac{p}{1-e}$ , set  $E, L_z$  equal to their Kerr values (which determines the velocity in the  $t$  and  $\phi$  directions), set  $u^r = 0$ , and determine  $u^\theta$  using the modulus of the 4-velocity. The upper and lower bounds on the deformation parameters determined in this way are shown in Fig. 10.  $M_{\text{KRZ}}$  is  $10^6 M_\odot$  and the total time is  $2 \times 10^6$  s.

### C. Orbits with radiative evolution

In the previous sections we only considered the geodesic orbits, which represents only a snapshot of EMRIs before

radiation reaction plays an important role. However, the stealth bias [33] can be broken by including radiation reaction, as we will discuss below. We use  $\nu$  to denote the mass ratio.

In this section, since we are considering the breaking of degeneracy by radiative evolution, the overlaps are maximized to give the fitting factor. For a given evolution time  $t_{\text{evo}}$  and two signals  $a(t)$  and  $b(t)$ , we input the two time series  $a(t)|_{t=0}^{t=t_{\text{evo}}}$  and  $b(t)|_{t=0}^{t=t_{\text{evo}}}$  with the designed power spectral density of LISA noise into the match function implemented in the PyCBC library [52].

As shown in Fig. 11, for equatorial orbits the pair of EMRI signals—which are degenerate when only geodesic orbits are considered—dephase with each other when radiation reaction is included. To illustrate the role of

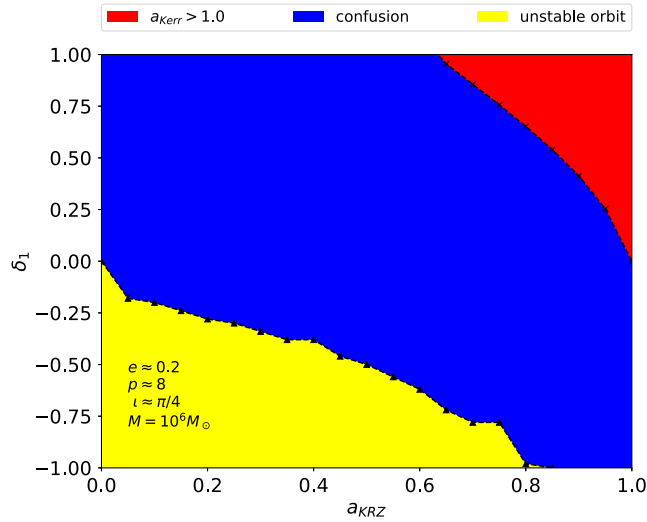


FIG. 10. The same as in Fig. 8 but for inclined orbits, and where the waveform at each point is determined by setting the initial  $E, L_z$  to be the same as in the corresponding Kerr orbit. See text for details.

radiation reaction in breaking the degeneracy, Fig. 12 shows the evolution of the fitting factor between two signals that are degenerate with each other in geodesic cases for different mass ratios. It is clear that the overlap

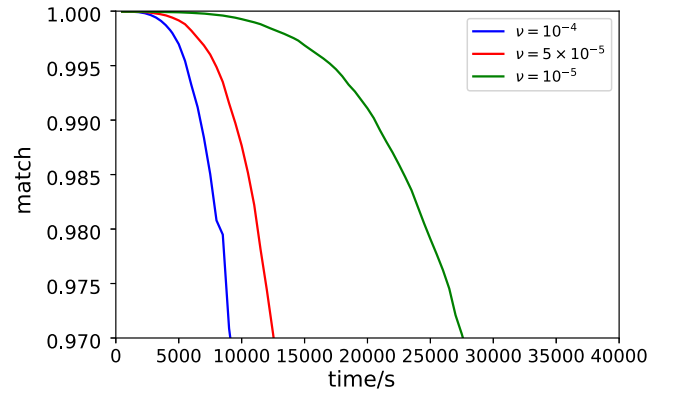


FIG. 12. Evolution of the fitting factor between EMRI signals with  $(\delta_1, a, M, e, p) = (0.2, 0.5, 200000, 0.5, 6)$  and  $(\delta_1, a, M, e, p) = (0, 0.617491, 201020, 0.5, 6)$  for different mass ratios ( $\nu$ ). Blue lines:  $\nu = 10^{-4}$ . Red lines:  $\nu = 5 \times 10^{-5}$ . Green lines:  $\nu = 10^{-5}$ .

drops below 0.97 within 30 000 s for the cases we considered with a central BH mass of about  $2 \times 10^5 M_\odot$ .

As shown in Fig. 13, for inclined orbits the EMRI signals with a mass ratio of  $10^{-4}$  break the degeneracy on a time scale of  $10^4 \sim 10^5$  seconds. The evolution of the fitting factor is shown in Figs. 14 and 15 for different mass ratios and semilatus, where the central BH mass is

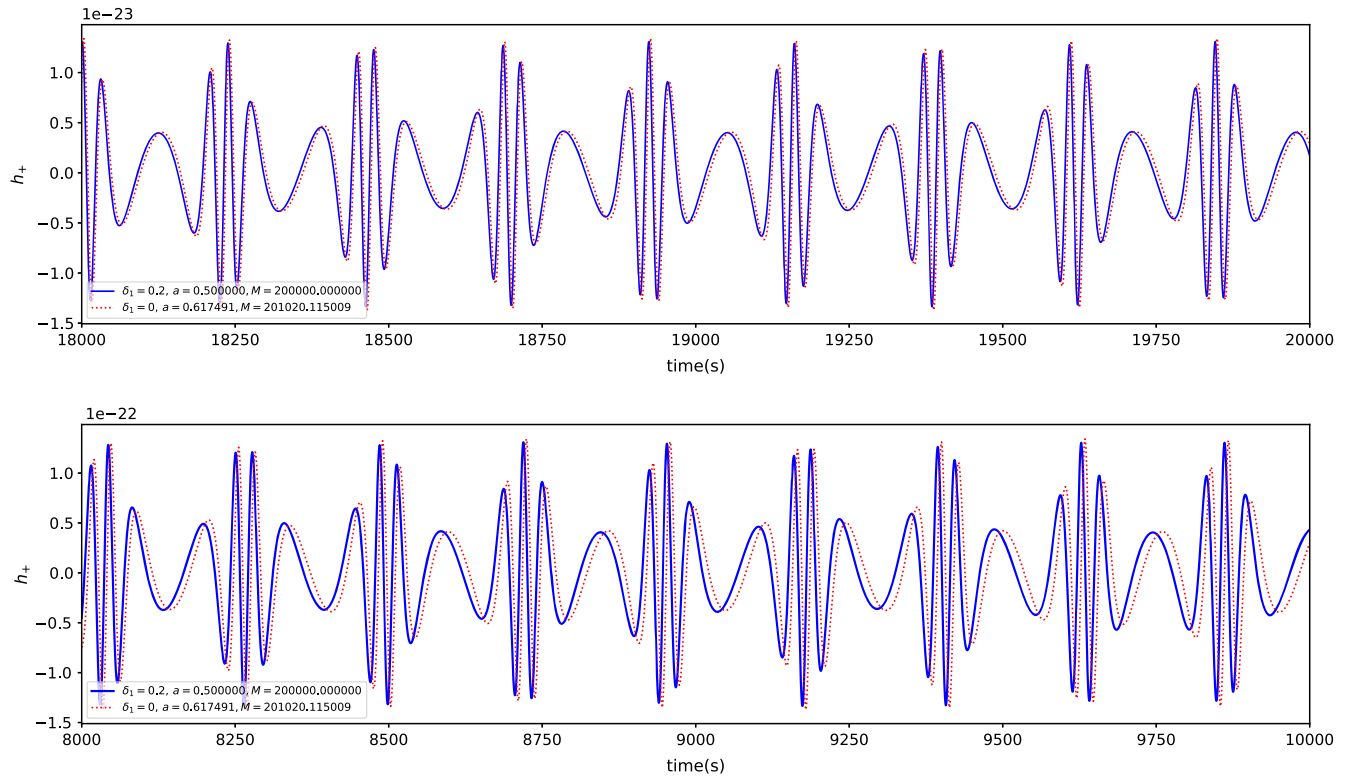


FIG. 11. Top panel: EMRI signals from geodesic orbits with  $(\delta_1, a, M, e, p) = (0.2, 0.5, 200000, 0.5, 6)$  (blue solid line) and  $(\delta_1, a, M, e, p) = (0, 0.617491, 201020, 0.5, 6)$  (red dotted line). Bottom panel: Same as in the top panel but for evolving orbits with a mass ratio of  $10^{-4}$ .

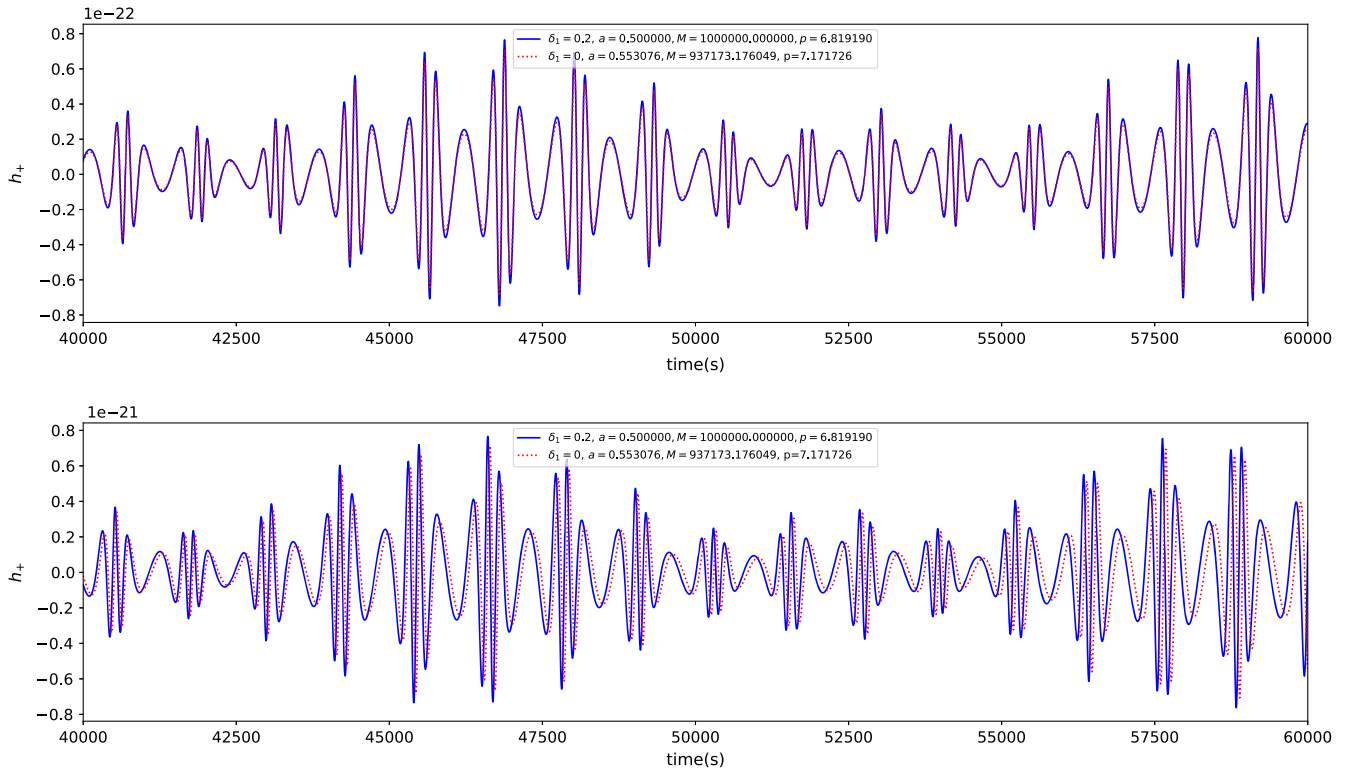


FIG. 13. Top panel: EMRI signals from geodesic orbits with  $(\delta_1, a, M, e, p, i) \approx (0.2, 0.5, 1000000, 0.432, 6.819, 0.780)$  (blue solid line) and  $(\delta_1, a, M, e, p, i) \approx (0, 0.553, 937173, 0.432, 7.172, 0.780)$  (red dotted line). Bottom panel: Same as in the top panel but for evolving orbits with a mass ratio of  $10^{-4}$ .

about  $10^6 M_\odot$ . The trend of the “dephasing time” (the time required for the overlap of signals to drop below 0.97) with respect to the mass ratio  $\nu$  is shown in Fig. 16. From the plot the approximate relation  $t \propto \frac{1}{\sqrt{\nu}}$  is clear. The systems with even smaller mass ratios [36,37] or that start with larger semilatus  $p$  may require up to years to break the degeneracy.

As a final comment, we note that we are considering systems where the small compact objects are relatively

close to the central BH, i.e., the semilatus  $p$  is small. The leading-order radiation fluxes are highly dependent on  $p$ , namely,  $\dot{E} \propto p^{-5}$ ,  $\dot{L}_z \propto p^{-7/2}$ . According to Fig. 16, the dephasing time has a strong dependence on the semilatus  $p$ . We expect that the effect of radiation would be much smaller when the waveform starts from an earlier stage of the EMRI with a larger separation. In these situations, the time required to break the degeneracy could be even longer.

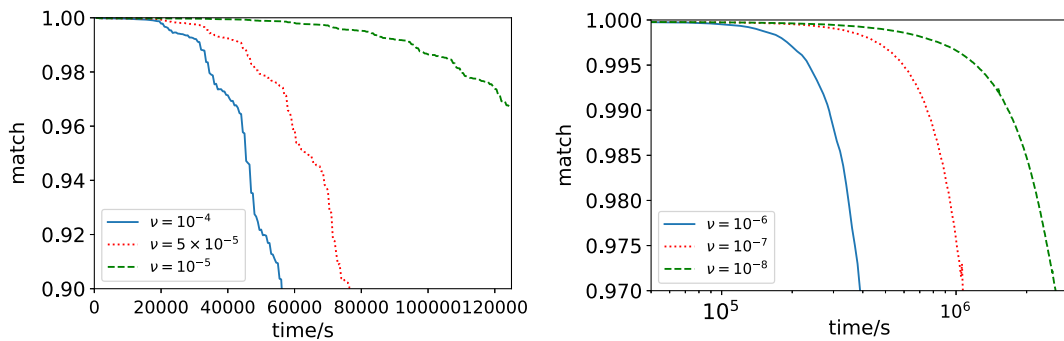


FIG. 14. Left panel: Evolution of the fitting factor between EMRI signals with  $(\delta_1, a, M, e, p, i) \approx (0.2, 0.5, 1000000, 0.432, 6.819, 0.780)$  and  $(\delta_1, a, M, e, p, i) \approx (0, 0.553, 937173, 0.432, 7.172, 0.780)$ . Blue solid line:  $\nu = 10^{-4}$ . Red dotted line:  $\nu = 5 \times 10^{-5}$ . Green dashed line:  $\nu = 10^{-5}$ . Right panel: Same as in the left panel, but for lower mass ratios. Blue solid line:  $\nu = 10^{-6}$ . Red dotted line:  $\nu = 10^{-7}$ . Green dashed line:  $\nu = 10^{-8}$ .

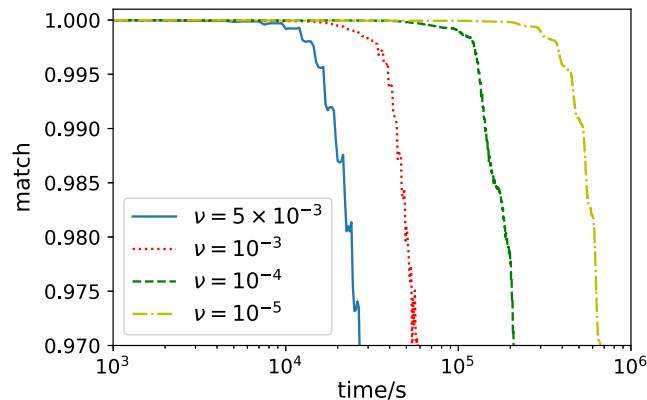


FIG. 15. Evolution of the fitting factor between EMRI signals with  $(\delta_1, a, M, e, p, i) \approx (0.2, 0.5, 1000000, 0.502, 12.020, 0.779)$  and  $(\delta_1, a, M, e, p, i) \approx (0, 0.538, 945615, 0.502, 12.511, 0.779)$  for different mass ratios  $\nu$ . Blue solid line:  $\nu = 5 \times 10^{-3}$ . Red dotted line:  $\nu = 10^{-3}$ . Green dashed line:  $\nu = 10^{-4}$ . Yellow dash-dotted line:  $\nu = 10^{-5}$ .

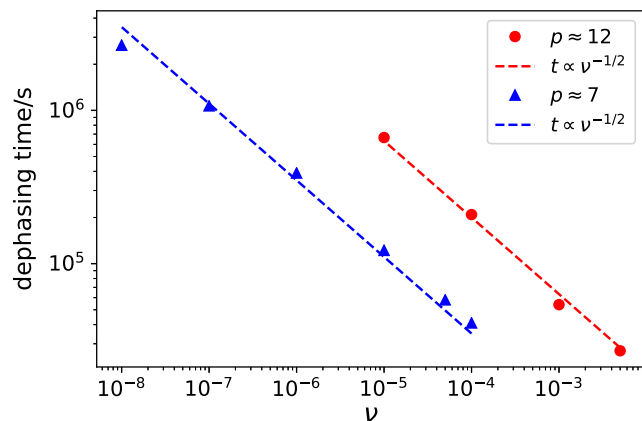


FIG. 16. The relation between the “dephasing time” (the time required for the fitting factor of two signals to drop below 0.97) and mass ratio  $\nu$ . Blue triangles: Match between signals defined by  $(\delta_1, a, M, e, p, i) \approx (0.2, 0.5, 1000000, 0.502, 12.020, 0.779)$  and  $(\delta_1, a, M, e, p, i) \approx (0, 0.538, 945615, 0.502, 12.511, 0.779)$ . Red dots: Match between signals defined by  $(\delta_1, a, M, e, p, i) \approx (0.2, 0.5, 1000000, 0.502, 12.020, 0.779)$  and  $(\delta_1, a, M, e, p, i) \approx (0, 0.538, 945615, 0.502, 12.511, 0.779)$ . Dashed lines are fitted scaling laws.

## V. CONCLUSION AND DISCUSSION

LIGO’s detections of GW signals have opened up the era of gravitational-wave physics and astronomy. Future LISA missions will be able to extend our observations over a broader spectrum of GW signals. One LISA’s scientific goals is to test the Kerr metric or no-hair theorem in the strong-field regime, but the “confusion problem” is still a challenge. In this paper, we considered the general

parametrized metric of axisymmetric BHs, namely, the KRZ metric. With a modified numerical kludge method for waveform generation, we investigated the confusion between GW signals emitted from orbits in the Kerr metric and KRZ non-Kerr metric. We mainly considered the deformation parameters  $\delta_1$  and  $\delta_2$  which represent the deformation of the Kerr metric components  $g_{tt}$  and  $g_{rr}$ , respectively. For both geodesic and evolving orbits, we studied the overlap between waveforms with the same orbital frequencies.

Although radiation reaction can break the degeneracy, the time required to break the degeneracy varies as the mass ratio changes. For mass ratios smaller than  $10^{-9}$  and starting with a larger semilatus  $p$ , this time could be comparable to the designed running time of LISA and the motion of the system can be approximated by geodesics. The results for geodesic orbits show that the confusion exists in a large range of the parameter space for both equatorial and inclined geodesics, within the small- and medium-deviation ( $\delta_i < 1$ ) regions. However, for high spin and a deviation  $\delta_i > 0$ , it is still possible to distinguish the background metric by imposing the physical restriction  $a_{\text{Kerr}} < 1$ . In the equatorial orbit cases, for given orbital parameters  $(e, p)$  the increase of  $\delta_i$  is almost equivalent to proportionally adding the spin and mass of a BH to the Kerr metric. This means that in most cases a waveform generated in the KRZ metric without radiative evolution can be mimicked by waveform templates with the Kerr black hole. This induces that one may not recognize deviations from the no-hair theorem. Therefore, when using short EMRI signals via the matched filtering method to test the Kerr spacetime, care must be taken to check for any confusion.

For systems where the confusion can be broken within a few days, we can use EMRI signals to test the no-hair theorem or the Kerr metric. The Fisher matrix can be exploited to estimate the extent to which the signal can constrain the non-Kerr parameters in alternative metrics. Similar studies have been done for several specific models [28,30]. In our future works, we will estimate the constraints that EMRI signals can put on parameters in a general parametrized metric.

One way to analyze data instantaneously or data from a system with a mass ratio smaller than about  $10^{-8}$  without stealth bias might be multimessenger measurements. It has been understood for a long time that x-ray emission (e.g., the iron line) can be used to measure BH spin [55], assuming the Kerr hypothesis. With the iron line, we are also able to put constraints on alternative metrics [56]. There has been some work constraining deformation in the JP metric [43], Johannsen metric [44], and KRZ metric [42]. EMRIs are extremely sensitive to small deviations, i.e., a 0.1% deviation of parameters could lead to a significant change in the overlap, but with degeneracy

between the deformation parameters, the BH spin, and mass. Graphically, the confidence level projected onto the  $(\delta_i, a, M)$  parameter space would be an infinitely long tube with narrow openings. By combining iron line data and GW signals, we can possibly break the degeneracy in the analysis. Naively thinking, while we can match the GW signal from a non-Kerr BH with parameters  $(\delta_i, a_{\text{KRZ}}, M_{\text{KRZ}})$  with a Kerr signal  $(0, a_{\text{Kerr}}, M_{\text{Kerr}})$ , the parameters  $(0, a_{\text{Kerr}}, M_{\text{Kerr}})$  might lie outside of the  $3\sigma$  level in the iron line fitting. Also, an accretion disk may have a large impact on the EMRI dynamics [57,58], although a simple model suggested that the degeneracy with Kerr spacetime will still exist if we consider the modification to the spacetime metric by a dust torus around a central BH [35].

## ACKNOWLEDGMENTS

This work is supported by NSFC No. 11773059, the Key Research Program of Frontier Sciences, CAS, No. QYZDB-SSW-SYS016, and MEXT, JSPS Leading-edge Research Infrastructure Program, JSPS Grant-in-Aid for Specially Promoted Research 26000005, JSPS Grant-in-Aid for Scientific Research on Innovative Areas 2905: JP17H06358, JP17H06361 and JP17H06364, JSPS Core-to-Core Program A. Advanced Research Networks, JSPS Grant-in-Aid for Scientific Research (S) 17H06133, the joint research program of the Institute for Cosmic Ray Research, University of Tokyo. This work made use of the High Performance Computing Resource in the Core Facility for Advanced Research Computing at Shanghai Astronomical Observatory.

- 
- [1] B. P. Abbott *et al.*, Observation of Gravitational Waves from a Binary Black Hole Merger, *Phys. Rev. Lett.* **116**, 061102 (2016).
- [2] B. P. Abbott *et al.*, GW170817: Observation of Gravitational Waves from a Binary Neutron Star Inspiral, *Phys. Rev. Lett.* **119**, 161101 (2017).
- [3] B. P. Abbott *et al.*, Multi-messenger observations of a binary neutron star merger, *Astrophys. J. Lett.* **848**, L12 (2017).
- [4] G. M. Harry (LIGO Scientific Collaboration), Advanced LIGO: The next generation of gravitational wave detectors, *Classical Quantum Gravity* **27**, 084006 (2010).
- [5] F. Acernese *et al.*, Advanced Virgo: A second-generation interferometric gravitational wave detector, *Classical Quantum Gravity* **32**, 024001 (2015).
- [6] K. Danzmann (LISA Study Team), LISA: Laser interferometer space antenna for gravitational wave measurements, *Classical Quantum Gravity* **13**, A247 (1996).
- [7] G. Hobbs *et al.*, The international pulsar timing array project: Using pulsars as a gravitational wave detector, *Classical Quantum Gravity* **27**, 084013 (2010).
- [8] <http://lisa.nasa.gov/>.
- [9] W.-R. Hu and Y.-L. Wu, The Taiji program in space for gravitational wave physics and the nature of gravity, *Natl. Sci. Rev.* **4**, 685 (2017).
- [10] J. Luo, L.-S. Chen, H.-Z. Duan, Y.-G. Gong, S. Hu, J. Ji, Q. Liu, J. Mei, V. Milyukov, M. Sazhin *et al.*, Tianqin: A space-borne gravitational wave detector, *Classical Quantum Gravity* **33**, 035010 (2016).
- [11] M. Armano *et al.*, Beyond the Required LISA Free-Fall Performance: New LISA Pathfinder Results Down to 20  $\mu\text{Hz}$ , *Phys. Rev. Lett.* **120**, 061101 (2018).
- [12] S. A. Hughes, Untangling the merger history of massive black holes with LISA, *Mon. Not. R. Astron. Soc.* **331**, 805 (2002).
- [13] K. Glampedakis and S. Babak, Mapping spacetimes with LISA: Inspiral of a test body in a ‘quasi-Kerr’ field, *Classical Quantum Gravity* **23**, 4167 (2006).
- [14] O. Dreyer, B. Kelly, B. Krishnan, L. S. Finn, D. Garrison, and R. Lopez-Aleman, Black-hole spectroscopy: Testing general relativity through gravitational-wave observations, *Classical Quantum Gravity* **21**, 787 (2004).
- [15] P. Amaro-Seoane, J. R. Gair, M. Freitag, M. C. Miller, I. Mandel, C. J. Cutler, and S. Babak, Intermediate and extreme mass-ratio inspirals—astrophysics, science applications and detection using LISA, *Classical Quantum Gravity* **24**, R113 (2007).
- [16] S. Babak, J. Gair, A. Sesana, E. Barausse, C. F. Sopuerta, C. P. L. Berry, E. Berti, P. Amaro-Seoane, A. Petiteau, and A. Klein, Science with the space-based interferometer LISA. V. extreme mass-ratio inspirals, *Phys. Rev. D* **95**, 103012 (2017).
- [17] C. P. L. Berry, S. A. Hughes, C. F. Sopuerta, A. J. K. Chua, A. Heffernan, K. Holley-Bockelmann, D. P. Mihaylov, M. C. Miller, and A. Sesana, The unique potential of extreme mass-ratio inspirals for gravitational-wave astronomy, [arXiv:1903.03686](https://arxiv.org/abs/1903.03686).
- [18] M. D. Hartl and A. Buonanno, Dynamics of precessing binary black holes using the post-Newtonian approximation, *Phys. Rev. D* **71**, 024027 (2005).
- [19] K. Glampedakis, Extreme mass ratio inspirals: LISA’s unique probe of black hole gravity, *Classical Quantum Gravity* **22**, S605 (2005).
- [20] W.-B. Han, Gravitational radiation from a spinning compact object around a supermassive Kerr black hole in circular orbit, *Phys. Rev. D* **82**, 084013 (2010).
- [21] W.-B. Han and Z. Cao, Constructing effective one-body dynamics with numerical energy flux for intermediate-mass-ratio inspirals, *Phys. Rev. D* **84**, 044014 (2011).
- [22] W.-B. Han, Gravitational waves from extreme-mass-ratio inspirals in equatorially eccentric orbits, *Int. J. Mod. Phys. D* **23**, 1450064 (2014).
- [23] W.-B. Han, Fast evolution and waveform generator for extreme-mass-ratio inspirals in equatorial-circular orbits, *Classical Quantum Gravity* **33**, 065009 (2016).

- [24] S. Babak, H. Fang, J.R. Gair, K. Glampedakis, and S.A. Hughes, “Kludge” gravitational waveforms for a test-body orbiting a Kerr black hole, *Phys. Rev. D* **75**, 024005 (2007).
- [25] L. Barack and C. Cutler, LISA capture sources: Approximate waveforms, signal-to-noise ratios, and parameter estimation accuracy, *Phys. Rev. D* **69**, 082005 (2004).
- [26] A. Ali, N. Christensen, R. Meyer, and C. Röver, Bayesian inference on EMRI signals using low frequency approximations, *Classical Quantum Gravity* **29**, 145014 (2012).
- [27] D. George and E. A. Huerta, Deep learning for real-time gravitational wave detection and parameter estimation: Results with advanced LIGO data, *Phys. Lett. B* **778**, 64 (2018).
- [28] P.D. Scharre and C.M. Will, Testing scalar-tensor gravity using space gravitational-wave interferometers, *Phys. Rev. D* **65**, 042002 (2002).
- [29] L. Barack and C. Cutler, Using LISA extreme-mass-ratio inspiral sources to test off-Kerr deviations in the geometry of massive black holes, *Phys. Rev. D* **75**, 042003 (2007).
- [30] C.J. Moore, A.J.K. Chua, and J.R. Gair, Gravitational waves from extreme mass ratio inspirals around bumpy black holes, *Classical Quantum Gravity* **34**, 195009 (2017).
- [31] J.R. Gair, M. Vallisneri, S.L. Larson, and J.G. Baker, Testing general relativity with low-frequency, space-based gravitational-wave detectors, *Living Rev. Relativity* **16**, 7 (2013).
- [32] L. Barack and C. Cutler, Confusion noise from LISA capture sources, *Phys. Rev. D* **70**, 122002 (2004).
- [33] M. Vallisneri and N. Yunes, Stealth bias in gravitational-wave parameter estimation, *Phys. Rev. D* **87**, 102002 (2013).
- [34] S. Vitale and W. Del Pozzo, How serious can the stealth bias be in gravitational wave parameter estimation, *Phys. Rev. D* **89**, 022002 (2014).
- [35] E. Barausse, L. Rezzolla, D. Petroff, and M. Ansorg, Gravitational waves from extreme mass ratio inspirals in nonpure Kerr spacetimes, *Phys. Rev. D* **75**, 064026 (2007).
- [36] P. Amaro-Seoane, X-mris: Extremely large mass-ratio inspirals, *Phys. Rev. D* **99**, 123025 (2019).
- [37] E.ourgoulhon, A. Le Tiec, . H. Vincent, and N. Warburton, Gravitational waves from bodies orbiting the galactic center black hole and their detectability by LISA, *Astron. Astrophys.* **627**, A92 (2019).
- [38] T. Johannsen and D. Psaltis, Metric for rapidly spinning black holes suitable for strong-field tests of the no-hair theorem, *Phys. Rev. D* **83**, 124015 (2011).
- [39] T. Johannsen, Regular black hole metric with three constants of motion, *Phys. Rev. D* **88**, 044002 (2013).
- [40] V. Cardoso, P. Pani, and J. Rico, On generic parametrizations of spinning black-hole geometries, *Phys. Rev. D* **89**, 064007 (2014).
- [41] R. Konoplya, L. Rezzolla, and A. Zhidenko, General parametrization of axisymmetric black holes in metric theories of gravity, *Phys. Rev. D* **93**, 064015 (2016).
- [42] Y. Ni, J. Jiang, and C. Bambi, Testing the Kerr metric with the iron line and the KRZ parametrization, *J. Cosmol. Astropart. Phys.* **16** (2016) 014.
- [43] T. Johannsen and D. Psaltis, Testing the no-hair theorem with observations in the electromagnetic spectrum. IV. relativistically broadened iron lines, *Astrophys. J.* **773**, 57 (2013).
- [44] C. Bambi, A. Cárdenas-Avedaño, T. Dauser, J. A. García, and S. Nampalliwar, Testing the Kerr black hole hypothesis using X-ray reflection spectroscopy, *Astrophys. J.* **842**, 76 (2017).
- [45] H. Krawczynski, Tests of general relativity in the strong-gravity regime based on X-ray spectropolarimetric observations of black holes in X-ray binaries, *Astrophys. J.* **754**, 133 (2012).
- [46] T. Johannsen, A. E. Broderick, P. M. Plewa, S. Chatzopoulos, S. S. Doeleman, F. Eisenhauer, V.L. Fish, R. Genzel, O. Gerhard, and M.D. Johnson, Testing General Relativity with the Shadow Size of Sgr A\*, *Phys. Rev. Lett.* **116**, 031101 (2016).
- [47] B. Carter, Global structure of the Kerr family of gravitational fields, *Phys. Rev.* **174**, 1559 (1968).
- [48] A.J.K. Chua, C.J. Moore, and J.R. Gair, Augmented kludge waveforms for detecting extreme-mass-ratio inspirals, *Phys. Rev. D* **96**, 044005 (2017).
- [49] L. S. Finn, Detection, measurement, and gravitational radiation, *Phys. Rev. D* **46**, 5236 (1992).
- [50] L. S. Finn, Detection, Measurement and Gravitational Radiation, *Phys. Rev. Lett.* **46**, 5236 (1992).
- [51] J.S. Read, C. Markakis, M. Shibata, K. Uryū, J.D.E. Creighton, and J.L. Friedman, Measuring the neutron star equation of state with gravitational wave observations, *Phys. Rev. D* **79**, 124033 (2009).
- [52] A. Nitz, I. Harry, and D. Brown, PyCBC software, v1. 7.11, Zenodo, 2017, <https://dx.doi.org/10.5281/zenodo.883086>.
- [53] A. Buonanno, B.R. Iyer, E. Ochsner, Y. Pan, and B.S. Sathyaprakash, Comparison of post-Newtonian templates for compact binary inspiral signals in gravitational-wave detectors, *Phys. Rev. D* **80**, 084043 (2009).
- [54] W. Schmidt, Celestial mechanics in Kerr spacetime, *Classical Quantum Gravity* **19**, 2743 (2002).
- [55] C.S. Reynolds, *Measuring Black Hole Spin Using X-ray Reflection Spectroscopy* (Springer, New York, 2015), pp. 277–294.
- [56] C. Bambi, Testing the space-time geometry around black hole candidates with the analysis of the broad  $K\alpha$  iron line, *Phys. Rev. D* **87**, 023007 (2013).
- [57] B. Kocsis, N. Yunes, and A. Loeb, Observable signatures of extreme mass-ratio inspiral black hole binaries embedded in thin accretion disks, *Phys. Rev. D* **84**, 024032 (2011).
- [58] N. Yunes, Imprint of Accretion Disk-Induced Migration on Gravitational Waves from Extreme Mass Ratio Inspirals, *Phys. Rev. Lett.* **107**, 171103 (2011).